PAPER • OPEN ACCESS

Theoretical design of mid-infrared interband cascade lasers in SiGeSn system

New Journal of Physics
The open access journal at the forefront of physics

Deutsche Physikalische Gesellschaft DPG
IOP Institute of Physics

Published in partnership with: Deutsche Physikalische Gesellschaft and the Institute of Physics

OPEN ACCESS

RECEIVED
11 March 2020

REVISED
2 June 2020

ACCEPTED FOR PUBLICATION
12 June 2020

PUBLISHED
21 August 2020

PAPER

Theoretical design of mid-infrared interband cascade lasers in SiGeSn system

Yuan Li[1], **Zhigang Song**[1], **Zeyu Li**[1], **Greg Sun**[2], **Chuan Seng Tan**[1], **Weijun Fan**[1] and **Qi Jie Wang**[1]

[1] School of Electrical and Electronic Engineering, Nanyang Technological University, 50 Nanyang Avenue, 639798, Singapore
[2] Department of Engineering, University of Massachusetts Boston, MA 02125, United States of America

E-mail: songzhigang198912@gmail.com and qjwang@ntu.edu.sg

Keywords: interband cascade laser, group-IV materials, eight-band $k{\cdot}p$ method

Abstract

By carefully analyzing the latest composition-dependent parameters of SiGeSn alloys, we come to realize that this system could provide type-II energy band alignment at direct bandgap condition. The discovery inspires us to explore the mid-infrared interband cascade laser (ICL) in SiGeSn system. Based on the eight-band $k \cdot p$ model, we theoretically design three schemes of ICL, in which the active region and the carrier injectors are optimized simultaneously. Afterward, the properties of TE-mode optical gain spectrums and differential gain are investigated individually for each scheme. Furthermore, the spontaneous emission spectrums and radiative current density are also calculated. Our theoretical results indicate that the active region composed of double-electron and triple-hole quantum wells has the best gain performance, reaching 660 cm^{-1} for a single period of the ICL under 7.8 $\times 10^{18}$ cm^{-3} injected electron density. This work opens up another type of infrared lasers that can be developed from the group-IV system, offering a new pathway to achieving the monolithic integration in Si photonics.

1. Introduction

Driven by the mature microelectronics industry, the CMOS-compatible silicon photonics, providing the possibility of monolithic optoelectronics integration, has been long pursued since 1990s [1–3]. Despite the great progress in Si-based waveguides, photodetectors and modulators, the inherent indirect-bandgap property of the elemental semiconductors Si and Ge has prevented them from being utilized for the development of efficient light emitters. Exploring efficient group-IV light sources has become a fundamental and challenging task for silicon photonics community. Since the unstrained GeSn alloy is observed to become a direct-bandgap semiconductor when Sn concentration exceeds about 8% [4, 5], the novel group-IV materials such as binary GeSn and ternary SiGeSn alloys have attracted great attention. In recent years, optically pumped lasing has been demonstrated by several groups from these group-IV alloys [6–11]. Compared to the type-I aligned bulk GeSn/SiGeSn heterostructure, the multiple quantum well (QW) structure could sharply lower the lasing threshold [12] as predicted in an earlier study [13]. All these progress have stimulated the exploration of electrically pumped lasers in group-IV system.

Besides the above-mentioned traditional interband laser, many efforts have also been devoted to the research of quantum cascade laser (QCL) in SiGe system [14–22]. Compared to the conduction band offset (CBO), the relatively larger valence band offset (VBO) prompted investigation of QCL schemes based on transitions between valence subbands [18], inspired by an early proposal [23]. Some other designs utilizing conduction subbands at Δ-valley [19] and L-valley [17] have also been proposed. Similar to QCLs, interband cascade laser (ICL) involving the recombination between electrons and holes offers a different kind of cascade configuration. Owing to the relatively longer upper-state carrier lifetime and voltage-efficient cascade scheme, ICL possesses higher quantum efficiency and lower threshold power density in comparison with QCLs. In fact, ICL has been widely investigated and show great potentials in

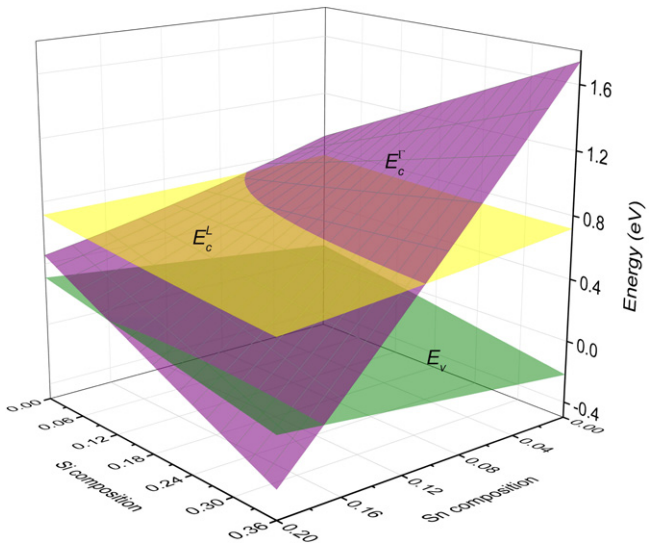

Figure 1. The energy band edges alignment of bulk $Si_xGe_{1-x-y}Sn_y$ alloy. The zero point energy is $E^{Ge}_{v,av}$. $E_v = E_{v,av} + \Delta/3$ is the valence band edge. E_c^Γ and E_c^L are the conduction band edges at Γ-valley and L-valley, respectively.

mid-infrared applications such as trace gas sensing, industrial process control and free-space optical communication [24–26]. However, to our best knowledge, the work on ICLs so far is only focused on InAs/GaSb system because of their type-II band alignment requirement. It is natural to raise a question: is it possible to realize ICL in group-IV system?

In this work, we theoretically investigate the possibility of ICL configurations in group-IV system. The eight-band $k \cdot p$ theory is utilized to design three specific ICL schemes based on the SiGeSn system. In order to facilitate the experimental community to take the designs as references, we have calculated the wavefunctions and energy levels associated with active region, electron and hole injectors. Furthermore, optical gain spectrums under different injection conditions and corresponding differential gain are investigated for the three schemes individually. Finally, because the spontaneous emission and radiative current density have a significant impact on the laser performance, we have studied their dependence on the different injection conditions. Our results confirm the feasibility of implementing ICLs in SiGeSn system and the gain coefficient of single period can reach 660 cm^{-1} under 7.8 $\times 10^{18}$ cm^{-3} injected carrier density.

2. Theoretical model

In group-IV system, Ge is an indirect-bandgap semiconductor whose conduction band minimum locates at L-valley, only 135 meV lower than Γ-valley. Sn atoms are commonly used to partially replace Ge atoms in GeSn alloy to lower down the conduction band at Γ-valley. With the increase of Sn concentration, GeSn alloy has the opportunity to become a direct-bandgap semiconductor that can be used for light source. For the multiple QW and superlattice based optoelectronic devices in group-IV system, Si can also be incorporated to increase the diversity of band alignment. The key parameter $E_{v,av}$ of $Si_xGe_{1-x-y}Sn_y$ ternary alloy, namely the averaged band offsets, can be written as

$$E_{v,\,av}(x,y) = (1-x-y)E^{Ge}_{v,\,av} + xE^{Si}_{v,\,av} + yE^{Sn}_{v,\,av}. \tag{1}$$

The parameters in equation (1) are adopted from reference [27], in which the $E_{v,av}$ are in best agreement with existing experimental data and/or *ab initio* theoretical calculations. Besides the averaged band offsets, the bandgap of $Si_xGe_{1-x-y}Sn_y$ alloy is another important parameter that does not strictly obey the Vegard's law. Generally, the compositional dependence of bandgap can be described by introducing the bowing effect [27],

$$E_t(x,y) = E_t^{Ge}(1-x-y) + E_t^{Si}x + E_t^{Sn}y - b^{GeSi}(1-x-y)x - b^{GeSn}(1-x-y)y - b^{SiSn}xy, \tag{2}$$

where $t = \Gamma, L$. As shown by equation (2), the quadratic compositional dependence is represented by the bowing coefficients b, whose values are adopted from reference [28] except b_Γ^{SiSn}. The determination of b_Γ^{SiSn}

Table 1. The main parameters of bulk Si, Ge and Sn at 300 K [27, 28]. The energy parameters are in eV and the lattice constant is in Å.

	$E_{v,av}$	Δ	E_g^Γ	E_g^L	m_c	γ_1	γ_2	γ_3	a_c^Γ	a_v	b_v	a_0
Si	−0.8	0.044	4.185	1.65	0.528	4.22	0.39	1.44	1.98	2.46	−2.1	5.4307
Ge	0.0	0.29	0.7985	0.664	0.038	13.38	4.24	5.69	−8.24	1.24	−2.9	5.6573
Sn	0.904	0.8	−0.413	0.092	−0.058	−15.0	−11.45	−8.55	−5.33	1.55	−2.7	6.4892

value is challenging, owing to the lattice mismatch would lower down the quality of SiSn alloys that hinders the measurement. In 2016, Wendav *et al* reported a much larger b_Γ^{SiSn} value (=24 eV) determined by photoluminescence experimentally [29], until last year Menendez *et al* obtained a similar result (=25.6 eV) by electroluminescence experimentally [27]. These researches confirmed the large bowing effect induced by the SiSn component. In this work, we refer to the updated parameters to design the band alignment. Taking the parameters from references [27, 28], figure 1 is plotted to display the energy band edges of bulk SiGeSn ternary alloys. As shown in figure 1, with the increase of Sn and Si compositions, E_c^Γ will be lower than E_c^L, which indicates the transition into a direct-bandgap semiconductor. Noticing that E_v is an inclined plane with the variation of alloy composition, there is a room near the intersecting lines between E_c^Γ and E_v to pick out the type-II broken-gap alignment at direct bandgap condition.

Whereafter, the envelope-function theory based on eight-band $k \cdot p$ model is utilized to design the band structures and wavefunctions of the ICL at Γ-valley. Since the SiGeSn alloy still holds the diamond crystal structure, the Hamiltonian used here is based on the Burt–Foreman theory, which takes account of the boundary conditions for superlattice [30]. The Pikus-Bir strain Hamiltonian is also incorporated as the way described in [31]. The total Hamiltonian can be written as

$$H = \begin{pmatrix}
E_c + A & 0 & -\sqrt{3}v & \sqrt{2}u & v^\dagger & 0 & u & \sqrt{2}v^\dagger \\
0 & E_c + A & 0 & -v & \sqrt{2}u & \sqrt{3}v^\dagger & \sqrt{2}v & -u \\
-\sqrt{3}v^\dagger & 0 & -P - Q & S_- & -R & 0 & \frac{S_-}{\sqrt{2}} & -\sqrt{2}R \\
\sqrt{2}u^\dagger & -v^\dagger & S_-^\dagger & -P + Q & -C & -R & \sqrt{2}Q & -\sqrt{\frac{3}{2}}\Sigma_- \\
v & \sqrt{2}u^\dagger & -R^\dagger & -C^\dagger & -P + Q & -S_+^\dagger & -\sqrt{\frac{3}{2}}\Sigma_+ & -\sqrt{2}Q \\
0 & \sqrt{3}v & 0 & -R^\dagger & -S_+ & -P - Q & \sqrt{2}R^\dagger & \frac{S_+}{\sqrt{2}} \\
u^\dagger & \sqrt{2}v^\dagger & \frac{S_-^\dagger}{\sqrt{2}} & \sqrt{2}Q^\dagger & -\sqrt{\frac{3}{2}}\sum_+^\dagger & \sqrt{2}R & -P - \Delta & -C \\
\sqrt{2}v & -u^\dagger & -\sqrt{2}R^\dagger & -\sqrt{\frac{3}{2}}\sum_-^\dagger & -\sqrt{2}Q^\dagger & \frac{S_+^\dagger}{\sqrt{2}} & -C^\dagger & -P - \Delta
\end{pmatrix} \tag{3}$$

where the details of each term in equation (3) can be found in references [32–34]. The bulk material parameters used for calculations are listed in table 1. All the calculations in this work are performed at 300 K. The numerical solutions are obtained by the plane-wave expansion method [28, 35].

Afterward, the TE-mode interband gain spectrums can be investigated under different injection conditions. For semiconductor lasers, the optical gain spectrum and spontaneous emission spectrum can be written as [36]

$$g(\hbar\omega) = \frac{\pi e^2}{n_r c \varepsilon_0 m_0^2 \omega} \sum_{m,n} \int_0^\infty \rho^{2\mathrm{D}} M_{m,n} (f_c^m - f_v^n) \mathcal{L}(\hbar\omega) \mathrm{d}E_t, \tag{4}$$

$$R_{\mathrm{sp}}(\hbar\omega) = \frac{\omega n_r e^2}{\pi c^3 \hbar \varepsilon_0 m_0^2} \sum_{m,n} \int_0^\infty \rho^{2\mathrm{D}} M_{m,n} f_c^m (1 - f_v^n) \mathcal{L}(\hbar\omega) \mathrm{d}E_t, \tag{5}$$

where $\mathcal{L}(\hbar\omega) = sech\left(\frac{E_{mn} + E_t - \hbar\omega}{\gamma}\right)/\gamma\pi$ is the broadening function which is more realistic than the Lorentzian lineshape [37]. $\rho^{2\mathrm{D}}$ is the two-dimensional density of state estimated by the parabolic energy band dispersion, $M_{m,n} = |\langle \psi_{cm} | \mathbf{e} \cdot \mathbf{p} | \psi_{vn} \rangle|^2$ is the momentum matrix element (MME) between the mth electron and the nth hole states. f_c^m and f_v^n are the Fermi–Dirac distribution for electrons and holes with quasi-Fermi levels $E_{f(c,v)}$, whose values are related to the carrier density and operating voltage. 2γ is the spectrum broadening factor, which is chosen to be 30 meV here. At last, the differential gain and radiative current density J_{rad} can be calculated by $\frac{\mathrm{d}g}{\mathrm{d}n}$ and $J_{\mathrm{rad}} = qL_z \int_0^\infty R_{\mathrm{sp}}(\hbar\omega)\mathrm{d}(\hbar\omega)$, respectively.

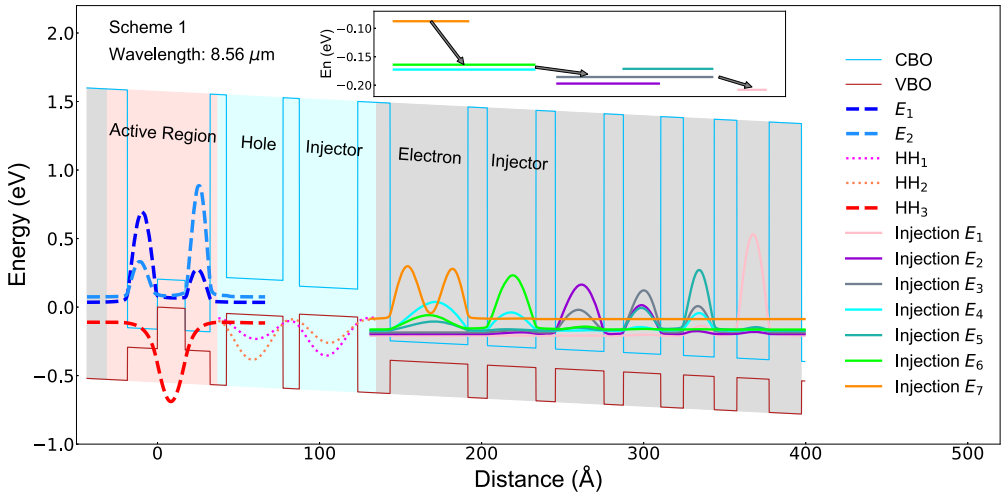

Figure 2. The design of SiGeSn system based ICL with W-type active region. The selected alloy compositions of active region are $Si_{0.4}Ge_{0.6}/Si_{0.32}Ge_{0.52}Sn_{0.16}/Ge_{0.82}Sn_{0.18}/Si_{0.32}Ge_{0.52}Sn_{0.16}/Si_{0.4}Ge_{0.6}$ (layer by layer sequentially). The applied electric field strength is 59 kV cm^{-1}. The states associated with the optical transition in active region (E_1, E_2 and HH_3) are shown by thick dashed curves. The states involved in carrier transportation in hole injector and electron injector are denoted by dotted and solid curves, respectively. The zoomed inset illustrates the carrier transport in electron injector. The vertical position (indicates energy levels) and the horizontal length (indicates wavefunction distribution) of the lines are plotted according to the calculations. The legends of Figures 3 and 4 as shown below are similar to the legends here.

3. Results and discussion

For ICL based on InAs/GaSb system, the W-type active region with two InAs electron QWs and one InGaSb hole QW has become a standard feature of the state-of-the-art ICL design and shown good performance experimentally. Hence, we inherit the basic concept there as the starting point and propose three types of ICL in SiGeSn system. In our design, the entire period of ICL including active region, electron and hole injectors are calculated simultaneously, from the viewpoint of practicability. All the three schemes are designed to emit at around 8.6 μm for easy comparison. As shown in figure 2, two electron QWs and one hole QW construct the W-type active region of the first scheme. The first and second electron (E_1 and E_2) wavefunctions both have the double-peaked shape due to the active region configuration. The third heavy-hole (HH_3) wavefunction is enclosed by the two ground state electron wavefunctions. The injected electrons recombine with holes in the active region and continue to flow into the injectors. The first and second heavy-hole (HH_1 and HH_2) are designed to reside in the hole injector and facilitate to the carrier transport. Specially, the HH_1 and HH_2 energy levels are carefully aligned to the most left E_7 energy level in electron injector for transport consideration. Meanwhile, the electron wavefunctions and energy levels in the electron injector are deliberately aligned as a staircase. The electron injector with multiple QWs design can provide the tunability of electron states, which guarantees the efficient carrier injection to the next period.

In contrary to the first design, the second scheme with the M-type active region composed of one electron QW and two hole QWs is proposed and shown in figure 3. Unlike the double-peaked electron wavefunctions in scheme one, here the wavefunctions of HH_1 and HH_3 labeled by the red and coral dashed curves are single-peaked and both contribute to the optical transition. Meanwhile, the HH_2 and HH_4 states denoted by the dotted curves in the hole injector couple the carriers in active region and in electron injector. The states in electron injector are also optimized for transport.

Enlighten by the above-proposed schemes, naturally the third design can be regarded as a combination: the active region contains two electron QWs and three hole QWs. To realize the double-peaked hole wavefunctions, the alloy composition of electron QWs has been refined to form a lower energy barrier for the hole states in active region. As a result, all of the first two electron and hole wavefunctions have the double-peaked shape as shown in figure 4. Here the design principle of injectors is similar to the above two schemes.

After demonstration of the specific energy states and wavefunctions for the proposed ICL schemes, the important optical gain properties are to be investigated here. Figures 5(a)–(c) illustrate the TE-mode optical gain spectrums of the three schemes under different injected electron density (IED), respectively. In calculations, the same quasi-Fermi level separation ($E_{fc} - E_{fv}$) is adopted for the three schemes for a straightforward comparison. At a rough glance, schemes 1 and 3 show the similar single-peaked gain

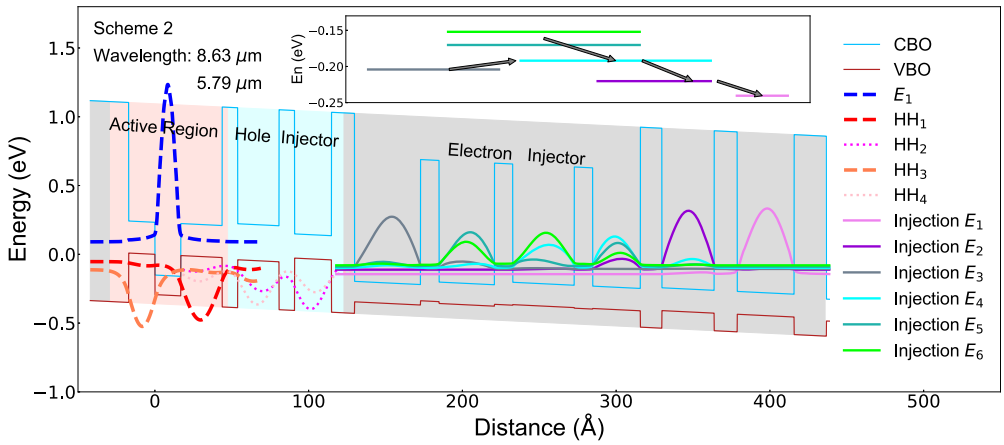

Figure 3. The design of SiGeSn system based ICL with M-type active region. Here the selected alloy compositions of active region are $Si_{0.2}Ge_{0.8}/Ge_{0.83}Sn_{0.17}/Si_{0.32}Ge_{0.52}Sn_{0.16}/Ge_{0.83}Sn_{0.17}/Si_{0.2}Ge_{0.8}$. The applied electric field strength is 54 kV cm^{-1}.

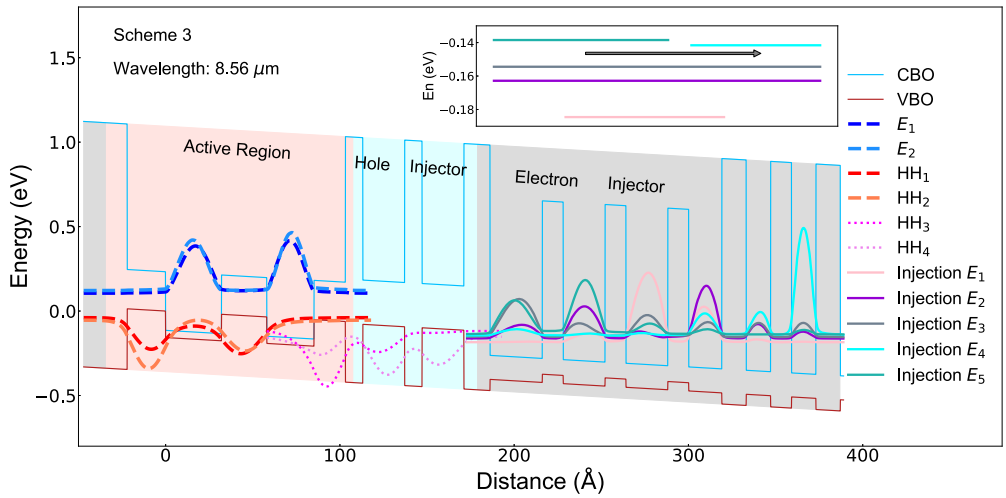

Figure 4. The design of SiGeSn system based ICL with multiple-QWs-type active region. Here the alloy compositions of active region are $Si_{0.2}Ge_{0.8}/Ge_{0.83}Sn_{0.17}/Si_{0.19}Ge_{0.63}Sn_{0.18}/Ge_{0.83}Sn_{0.17}/Si_{0.19}Ge_{0.63}Sn_{0.18}/Ge_{0.83}Sn_{0.17}/Si_{0.2}Ge_{0.8}$. The applied electric field strength is 60 kV cm^{-1}.

spectrum profile, whereas the gain spectrum profile of scheme 2 possesses the broadband characteristic. The distinct gain profile difference can be explained by the much different quantum transition characteristics of the three schemes. Let us decompose the gain spectrum formula described by equation (4) to find the reason. MME and carrier occupation difference (COD) play essential roles in gain profile generation. Therefore, we calculate the MME, COD and their product at zero wavevector for the three schemes, individually. As demonstrated in figure 6, the MME and COD cannot always reach maximum at the same optical transition. Taking scheme 2 for example, the E_1–$HH_{1,3}$ and E_2–$HH_{1,3,4}$ transitions all have considerable MME strength. However, considering the carrier occupation aspect, the E_2–$HH_{1,3,4}$ transitions are much more ineffective than the others. Hence these three transitions hardly contribute to the overall optical gain spectrum, as indicated in figure 6(h). As a result, the E_1–HH_1 and E_1–HH_3 transitions construct the main gain profile of scheme 2, E_1–HH_2 transition does a small contribution as well. The similar analysis can be performed to scheme 1 and 3 as well. As a result, we determine that the E_1–HH_3 transition leads to the gain profile of scheme 1; the E_1–HH_1 transition forms the main gain profile of scheme 3, other transitions merely contribute to the small gain profile broadening on the right-side.

Now let us investigate the gain spectrum evolution with the IED variation. As shown in figures 5(a)–(c), with the gradual increase of electron density, the gain spectrum intensity of all the three schemes experience an increase and then a decrease. In order to get a deeper insight into this phenomenon, we calculate the variation of maximum gain and differential gain with the increase of IED, as displayed in figures 5(d)–(f). Apparently, the maximum gain curves of all the three schemes show a concave shape plotted by the light blue lines, accompanied with the differential gain curves go across the zero point plotted by the coral lines.

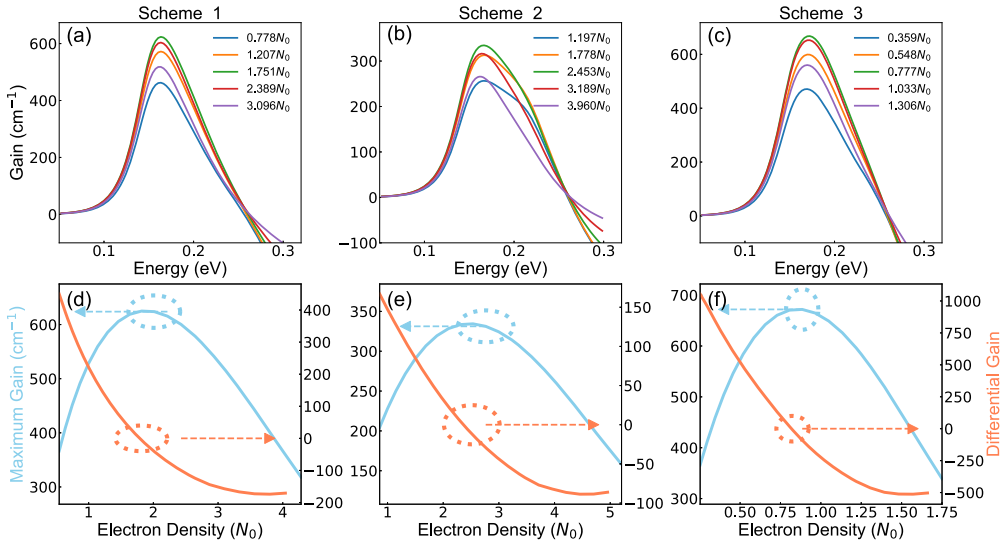

Figure 5. (a)–(c) are the TE-mode optical gain spectrums calculated by equation (4) of the three schemes, respectively. Here five different IED in the active region are considered. $N_0 = 1.0 \times 10^{19}$ cm^{-3} is the unit of IED. (d)–(f) depict the maximum value of the optical gain spectrums and corresponding differential gain $\frac{\mathrm{d}g}{\mathrm{d}n}$ vs IED, for the three schemes, respectively. $E_{\mathrm{fc}} - E_{\mathrm{fv}} = \hbar\omega_0 + 4.5\ k_{\mathrm{B}}T$ is adopted in calculations.

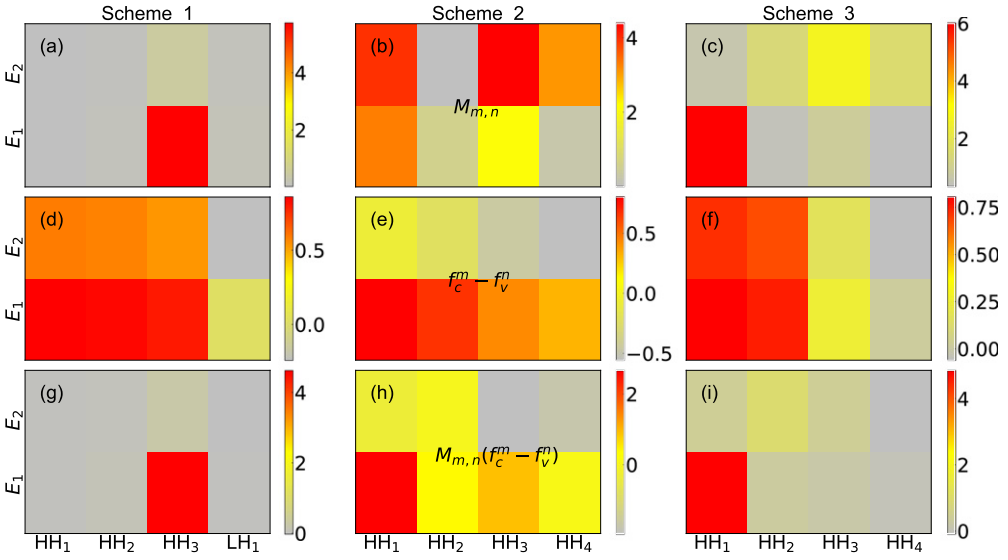

Figure 6. (a)–(c) are the MME ($M_{m,n}$) of the three proposed schemes, respectively; (d)–(f) are the COD ($f_c^m - f_v^n$) of the three schemes, respectively; (g)–(i) are the product of MME and COD for the three schemes, respectively. In calculation, the IED for the three schemes are 1.751 N_0, 2.453 N_0 and 0.777 N_0, respectively.

It indicates there exists an inflection point for the maximum gain curve. The critical electron density can be extracted from the differential gain curve by setting the differential gain value to zero, as depicted by the coral dash circles in figures 5(d)–(f). The critical point gives out the optimal IED, beyond which the optical gain intensity would start to drop down. The occurrence of inflection point can be explained by the electron and hole occupation states For the bipolar lasers such as ICL, actually the amount of effective electron–hole pairs in the active region determines the optical gain intensity. When the ICL is working, $E_{\mathrm{fc}} - E_{\mathrm{fv}} = qFL$ is established under quasi-equilibrium condition, where F and L are the electric field strength and one period length respectively [26]. In the situation here, E_{fc} would be lifted up by the increased electron density in the active region, consequently E_{fv} would also be moved toward the conduction band direction dues to keep a constant quasi-Fermi level separation. If E_{fv} is far beyond the hole energy levels in the active region, there would be no enough holes provided for the radiative recombination. Therefore, the inflection point phenomenon of the optical gain occurs here.

Comparing the optical gain spectrums of the three proposed schemes, it is obvious that scheme 3 possesses the strongest gain intensity per IED investigated. Specifically, the maximum gain of scheme 3 can

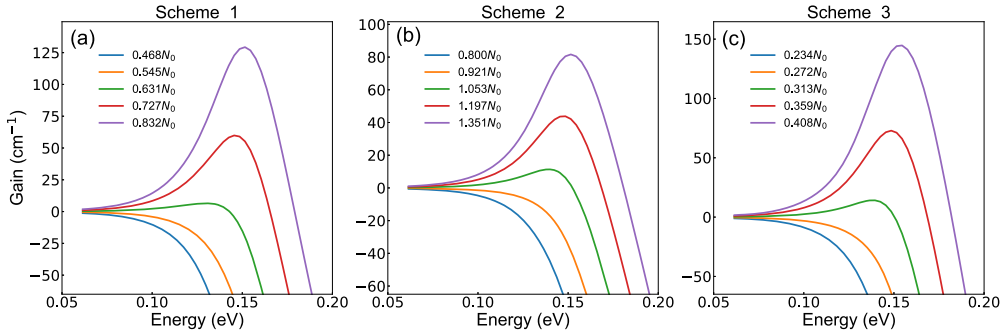

Figure 7. (a)–(c) are the TE-mode optical gain spectrums of the proposed three schemes near the threshold condition, respectively. Here we set $E_{fc} - E_{fv} - \hbar\omega_0 = mk_BT$ and $E_{fc} - E_1 = \frac{m}{2} k_BT$. m is set to be equal-step increased in the range $[-0.2, 1.6]$. The corresponding IEDs are shown in the legends.

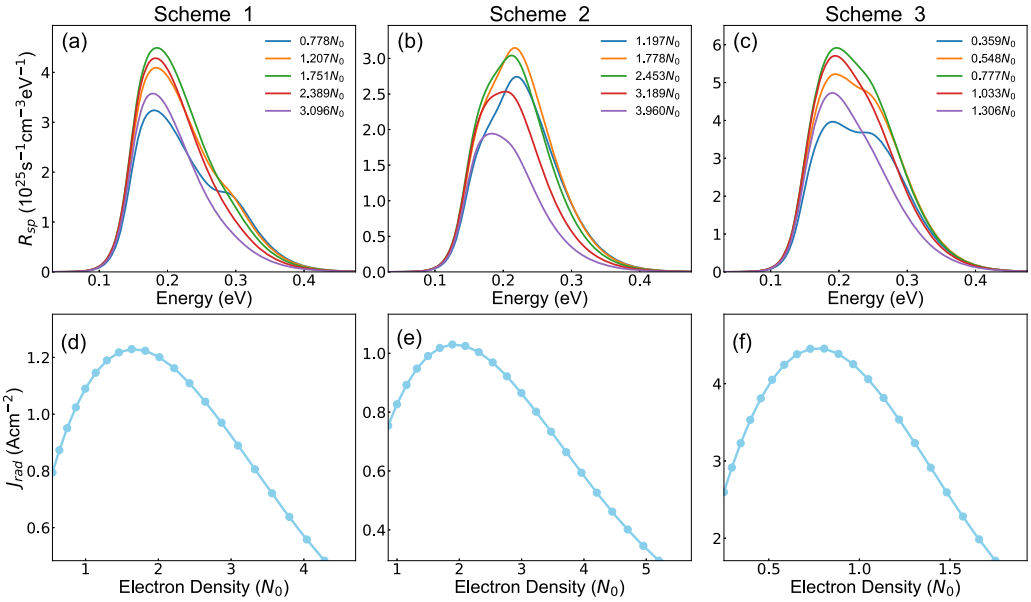

Figure 8. (a)–(c) are the spontaneous emission spectrums of the three schemes calculated by equation (5), under five different IED. (d)–(f) describe the radiative current density of the three schemes with IED variation.

reach 660 cm^{-1} under 0.78 $\times 10^{19}$cm^{-3} IED; whereas, to reach a similar level of maximum gain, scheme 1 needs 1.75 $\times 10^{19}$cm^{-3} IED; scheme 2 does not have the ability to do so. On the other hand, by further optimizing different transitions induced optical gain, scheme 2 provides the possibility to realize the flat broadband gain profile and then benefits to the exploration of optical frequency comb in SiGeSn system. Besides, scheme 2 could be used as the dual-wavelength laser by further separating the optical transitions in gain profile.

In addition, the TE-mode optical gain spectrums of the three schemes under lower carrier density are also investigated. Here we set $E_{fc} - E_{fv} < \hbar\omega_0$ as the starting point, then we equally move the quasi-Fermi levels toward the opposite direction to gradually increase the energy separation until the optical gain occurs. As shown in figure 7, all the lowest-energy transitions for the three schemes evolve from absorption to gain with the increased IED. Whereas the higher energy transitions have the absorption characteristic. The reason is the quasi-Fermi level separation provides the capability of optical gain [36], here the adopted maximum separation is only $\hbar\omega_0 + 1.6k_BT$, which cannot drive enough optical gain of the higher energy transitions. The transparency electron densities are extracted from figure 7 as well, the values are about 0.631, 1.053 and 0.313 $\times 10^{19}$cm^{-3} for the three schemes, respectively. For a more realistic consideration, assuming the ICL is fabricated into a 3 mm long Fabry–Perot waveguide, the threshold material gain for a seven-stage ICL is roughly estimated to be 55 cm^{-1}, under the assumption that the total optical confinement is about 0.3 [13], the effective refractive index is about 4 and the cavity loss is about 13 cm^{-1}.

At last, the spontaneous emission spectrums and radiative current density corresponding to figure 5's injection condition are investigated. As shown in figure 8(a)–(c), the spontaneous emission spectrums

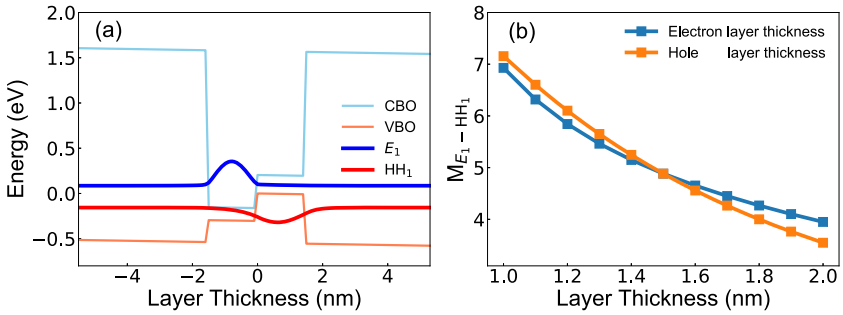

Figure A1. (a) The energy bands and wavefunctions for a basic four-layer ($Si_{0.4}Ge_{0.6}/Si_{0.32}Ge_{0.52}Sn_{0.16}/Ge_{0.82}Sn_{0.18}/Si_{0.4}Ge_{0.6}$) QWs structure. The applied electric field strength is 59 kV cm^{-1}. (b) The $M_{E_1-HH_1}$ with the thickness variation of either the electron or the hole QW.

always keep the positive values. Scheme 1 is able to show the shoulder like profile, whereas the spectrums of scheme 3 show the slightly broadband characteristic. Schemes 1 and 2 have a smaller radiative current density than scheme 3, which may mean the lower power consumption from engineering viewpoint. Furthermore, the radiative current density of the three schemes also present the inflection point phenomenon with IED variation, which could provide guidance for practical design as well. The characteristics of spontaneous emission spectrums and radiative current density can be explained in a similar method as that for the gain spectrums, but not expanded here.

Although three designs of ICL based on SiGeSn system are proposed in this work, it still takes great effort to realize the ICL experimentally. The main concern is the challenging material growth tricks of SiGeSn alloys. With the endeavor of material scientists, GeSn alloy with Sn composition up to 33% has been synthesized by the chemical vapor deposition technique recently [38]. The progress in the material growth of SiGeSn alloys, could speed up the development of group-IV based devices. For the theoretical aspect, a more complicated 30-band $k \cdot p$ method can be developed to explore the inter-valley transfer problems in SiGeSn based low-dimensional structures [39]. The more precise transport model based on non-equilibrium Green's function and density matrix theories are also required to be explored for the SiGeSn based ICL [21, 40].

4. Conclusion

In summary, we propose three mid-infrared ICL designs in SiGeSn system and theoretically analyze their lasing feasibility based on a type-II band alignment that can be achieved with SiGeSn alloys in direct bandgap condition.The active region with double-electron and triple-hole QWs shows the best optical gain performance. The M-type active region has the possibility to become the platform for optical frequency comb. The optical gain and spontaneous emission of the proposed schemes exhibit distinct spectral profiles. Furthermore, the maximum gain spectrum and radiative current density show the inflection point phenomenon. Our design work brings forward a new kind of lasers that can be explored and potentially implemented monolithically in silicon photonics.

Acknowledgments

This work is supported by the funding from Singapore National Research Foundation, Competitive Research Program (NRF-CRP19-2017-01), and Ministry of Education, Singapore Grant (MOE2016-T2-2-159, MOE2018-T2-1-176). Greg Sun acknowledges the support from Air Force Office of Scientific Research (FA9550-19-1-0341). WJ Fan acknowledges the National Supercomputing Center of Singapore for the calculation resource support.

Appendix A

As a supplement, we calculate the momentum matrix element between E_1 and HH_1 states ($M_{E_1-HH_1}$) of a basic type-II interface structure in SiGeSn system. As shown in figure A1(a), the single electron and hole QWs surrounded by two barriers on both sides construct the four-layer structure. By changing the thickness of either of the two QWs, as demonstrated in figure A1(b), the momentum matrix elements increase monotonously with the decrease of QW thickness.

References

[1] Soref R A 1993 *Proc. IEEE* **81** 1687–706
[2] Soref R 2010 *Nat. Photon.* **4** 495
[3] Soref R, Buca D and Yu S Q 2016 *Opt. Photonics News* **27** 32–9
[4] Ghetmiri S A *et al* 2014 *Appl. Phys. Lett.* **105** 151109
[5] Wirths S *et al* 2015 *Nat. Photon.* **9** 88
[6] Al-Kabi S *et al* 2016 *Appl. Phys. Lett.* **109** 171105
[7] Margetis J *et al* 2017 *ACS Photonics* **5** 827–33
[8] Margetis J *et al* 2018 *Appl. Phys. Lett.* **113** 221104
[9] von den Driesch N *et al* 2018 *Adv. Sci.* **5** 1700955
[10] Thai Q M *et al* 2018 *Opt. Express* **26** 32500–8
[11] Zhou Y *et al* 2019 *ACS Photonics* **6** 1434–41
[12] Stange D *et al* 2018 *ACS Photonics* **5** 4628–36
[13] Sun G, Soref R and Cheng H 2010 *Opt. Express* **18** 19957–65
[14] Soref R A and Sun G 2001 *Appl. Phys. Lett.* **79** 3639–41
[15] Bormann I, Brunner K, Hackenbuchner S, Zandler G, Abstreiter G, Schmult S and Wegscheider W 2002 *Appl. Phys. Lett.* **80** 2260–2
[16] De Rossi A, Carras M and Paul D J 2006 *IEEE J. Quantum Electron.* **42** 1233–8
[17] Sun G, Cheng H, Menendez J, Khurgin J B and Soref R 2007 *Appl. Phys. Lett.* **90** 251105
[18] Paul D, Matmon G, Townsend P, Zhang J, Zhao M and Ni W X 2007 *IETE J. Res.* **53** 285–92
[19] Valavanis A, Lever L, Evans C, Ikonić Z and Kelsall R 2008 *Phys. Rev.* B **78** 035420
[20] Lever L, Valavanis A, Ikonić Z and Kelsall R 2008 *Appl. Phys. Lett.* **92** 021124
[21] Grange T *et al* 2019 *Appl. Phys. Lett.* **114** 111102
[22] Ciano C *et al* 2020 *Opt. Express* **28** 7245–58
[23] Sun G, Friedman L and Soref R A 1995 *Appl. Phys. Lett.* **66** 3425–7
[24] Yang R Q, Hill C J and Yang B 2005 *Appl. Phys. Lett.* **87** 151109
[25] Vurgaftman I, Bewley W, Canedy C, Kim C, Kim M, Merritt C, Abell J, Lindle J and Meyer J 2011 *Nat. Commun.* **2** 585
[26] Vurgaftman I *et al* 2015 *J. Phys. D: Appl. Phys.* **48** 123001
[27] Menendez J, Wallace P, Xu C, Senaratne C, Gallagher J and Kouvetakis J 2019 *Mater. Today: Proc.* **14** 38–42
[28] Zhu Y H, Xu Q, Fan W J and Wang J W 2010 *J. Appl. Phys.* **107** 073108
[29] Wendav T *et al* 2016 *Appl. Phys. Lett.* **108** 242104
[30] Foreman B A 1993 *Phys. Rev.* B **48** 4964
[31] Bir G and Pikus G 1974 *Symmetry and Strain-Induced Effects in Semiconductors A Halsted Press Book* (New York: Wiley)
[32] Foreman B A 1997 *Phys. Rev.* B **56** R12748
[33] Liu G and Chuang S L 2002 *Phys. Rev.* B **65** 165220
[34] Li Y, Liu F, Ye X, Liu Y, Wang J and Chen Y 2019 *J. Appl. Phys.* **126** 065704
[35] Li S S, Xia J B, Yuan Z, Xu Z, Ge W, Wang X R, Wang Y, Wang J and Chang L 1996 *Phys. Rev.* B **54** 11575
[36] Chaung S 2009 *Physics of Photonic Devices* (New York: Wiley)
[37] Chow W W, Koch S W and Sargent III M 1994 *Semiconductor-Laser Physics* (Berlin: Springer)
[38] Xu C, Ringwala D, Wang D, Liu L, Poweleit C D, Chang S L, Zhuang H L, Menéndez J and Kouvetakis J 2019 *Chem. Mater.* **31** 9831–42
[39] Song Z, Fan W, Tan C S, Wang Q, Nam D, Zhang D H and Sun G 2019 *IEEE J. Quantum Electron.* **56** 1–8
[40] Iotti R C and Rossi F 2020 *Appl. Sci.* **10** 1114